

MODELING THE PAN-SPECTRAL ENERGY DISTRIBUTION OF STARBURST GALAXIES. IV. THE CONTROLLING PARAMETERS OF THE STARBURST SED

BRENT GROVES,¹ MICHAEL A. DOPITA,² RALPH S. SUTHERLAND,² LISA J. KEWLEY,³ JÖRG FISCHERA,⁴
CLAUS LEITHERER,⁵ BERNHARD BRANDL,¹ AND WIL VAN BREUGEL⁶

Received 2007 August 31; accepted 2007 December 8

ABSTRACT

We combine the stellar spectral synthesis code Starburst99, the nebular modeling code MAPPINGS III and a one-dimensional dynamical evolution model of H II regions around massive clusters of young stars to generate improved models of the spectral energy distribution (SED) of starburst galaxies. We introduce a compactness parameter, \mathcal{C} , which characterizes the specific intensity of the radiation field at ionization fronts in H II regions and which controls the shape of the far-infrared (IR) dust reemission, often referred to loosely as the dust “temperature.” We also investigate the effect of metallicity on the overall SED and in particular, on the strength of the polycyclic aromatic hydrocarbon (PAH) features. We provide templates for the mean emission produced by the young compact H II regions, the older (10–100 Myr) stars and for the wavelength-dependent attenuation produced by a foreground screen of the dust used in our model. We demonstrate that these components may be combined to produce an excellent fit to the observed SEDs of star formation–dominated galaxies which are often used as templates (Arp 220 and NGC 6240). This fit extends from the Lyman limit to wavelengths of about 1 mm. The methods presented in both this paper and in the previous papers of this series allow the extraction of the physical parameters of the starburst region (star formation rates, star formation rate history, mean cluster mass, metallicity, dust attenuation, and pressure) from the analysis of the pan-spectral SED.

Subject headings: dust, extinction — galaxies: general — galaxies: starburst — H II regions —
infrared: galaxies — radio continuum: galaxies — stars: formation — ultraviolet: galaxies

Online material: color figures

1. INTRODUCTION

By definition, the bolometric luminosity of a starburst galaxy is dominated by the young stars it contains. Thus, regardless of how much or how little of this luminosity is reprocessed through the dusty interstellar medium (ISM), either through thermal emission in the infrared (IR) of dust grains, through fluorescent processes, or through heating and reemission in an ionized medium, the pan-spectral spectral energy distribution (SED) encodes information about what the star formation rate currently is and what it has been in the recent past. The first objective of pan-spectral SED modeling is therefore to be able to reliably infer star formation rates in galaxies and to provide likely error estimates using observational data sets which may in practice be restricted to only certain emission lines or spectral features. In principle, almost any part of the SED of a starburst can be used as a star formation indicator, provided that the appropriate bolometric correction to the absolute luminosity can be made, and observational issues are accounted for. In practice, each wavelength regime has a different level of sensitivity to the ongoing star formation which is dependent on these bolometric corrections, with hydrogen emission lines and the IR part of the SED being the most robust indicators

of the current star formation rate (SFR). These bolometric corrections critically depend on the foreground dust absorption (more properly called dust attenuation), and the geometry of the embedded dusty molecular clouds, with respect to both the ionizing stars and the older stellar population. The accurate determination of such bolometric corrections is a major motivation of our theoretical work of pan-spectral SED modeling.

In order to correctly model the SEDs of starburst galaxies, we first need to understand how the form of the SED is controlled by the interstellar physics and the geometry of the stars with respect to the gas. Once these are understood, we can then use our theoretical models to attain the objectives of our second motivation for such SED modeling; to gain insights into the physical parameters of starburst galaxies. In particular, we can hope to quantify the stellar populations, the atomic and molecular gas content, the star and gas-phase metallicities, physical parameters of their ISM such as the pressure or mean density, and the nature of the interstellar dust, both its composition and spatial distribution. The physical parameters so derived on homogeneous samples of objects can then help develop our insight into the physical processes which control them.

The dust grain temperature distribution and, therefore, the shape and peak of the far-IR feature, depends critically on the geometrical relationship between the dust grains and the stellar heating sources assumed in the model. Models with warmer far-IR colors will have a more compact disposition of gas with respect to the stars. The difficulty here is that, in any simple starburst model, these geometrical relationships are not determined a priori.

In the semiempirical modeling of Dale et al. (2001) and Dale & Helou (2002), the SEDs of both disk and starburst galaxies were suggested to form a one-parameter family in terms of dust temperature. This suggested that starburst galaxies have hotter

¹ Sterrewacht Leiden, Leiden University, P.O. Box 9513, 2300 RA Leiden, The Netherlands.

² Research School of Astronomy and Astrophysics, The Australian National University, Cotter Road, Weston Creek, ACT 2611, Australia.

³ University of Hawai‘i, Institute for Astronomy, 2680 Woodlawn Drive, Honolulu, HI 96822.

⁴ Canadian Institute for Theoretical Astrophysics, University of Toronto, 60 Saint George Street, Toronto, ON, M5S 3H8, Canada.

⁵ Space Telescope Science Institute, 3700 San Martin Drive, Baltimore, MD 21218.

⁶ University of California at Merced, P.O. Box 2039, Merced, CA 95344.

dust temperatures. Lagache et al. (2003) (again empirically) have suggested that the absolute luminosity controls the form of the SED. Both of these assertions may be true to some extent, since IR luminous galaxies generally have greater rates of star formation than normal galaxies.

Galliano et al. (2003) take the simplest approach of approximating the starburst by a spherical H II region and clumpy dust shell around the central star-forming region. A more advanced approach is used by Siebenmorgen & Krügel (2007) to model starbursts and ultraluminous infrared galaxies (ULIRGs). While assuming a spherical geometry for the radiative transfer, they also include the effect of the hot dust around young OB stars as well as the diffuse ISM dust surrounding the starburst and older stellar population. The hot dust component is important as it can dominate the mid-IR emission (Krügel & Siebenmorgen 1994).

Associated with the latter models is the approach by Efstathiou et al. (2000). Likewise concentrating on starburst galaxies, they modeled the starburst as a group of stars surrounded by thick molecular clouds in a manner similar to our approach, and in addition, also included a similar, simple description for the evolution of the distance of the molecular clouds to the illuminating stars. With these models they could explain the observed *IRAS* distributions and reproduce several *Infrared Space Observatory (ISO)* observations.

One of the more sophisticated approaches is taken in the GRASIL code by the Padova-Trieste group (Silva et al. 1998; Granato et al. 2000). Their starburst model uses a spherical geometry with King profiles, and they allow for the formation of clusters of stars in molecular complexes, and their subsequent escape from these regions. This group has since incorporated gas physics by use of the Cloudy code (Ferland et al. 1998; Abel et al. 2005) to provide emission-line diagnostics as well as dust continuum diagnostics (Panuzzo et al. 2003). A similarly advanced approach was used by Piovani et al. (2006a, 2006b), who also assume a spherical geometry with King profiles and young stars in molecular complexes.

In the conceptually sophisticated models of Tagaki et al. (2003a, 2003b) a mass-radius relationship for the star formation region of $r_i/\text{kpc} = \Theta(M/10^9 M_\odot)^{1/2}$ is adopted along with a stellar density distribution given by a generalized King profile. The parameter Θ is a compactness parameter which expresses the degree of matter concentration, and is related to the optical depth of the dust through which the starburst region is seen. For a sample of ultraluminous starbursts, they find that, while most conform to a constant surface brightness of order $10^{12} L_\odot \text{kpc}^{-2}$, there are a few objects with surface brightnesses roughly 10 times larger than this, which they ascribe to postmerger systems. In this paper, we adopt a derivative version of this concept of a compactness parameter as the factor which provides the main control on the shape of the far-IR bump.

All the fully theoretical (as opposed to semiempirical) methods used by other groups involve the calculation of essentially a single spherical radiation transfer problem. Unfortunately, real starburst galaxies have many separate clusters of many different ages distributed in a complex spatial distribution. However, gas column densities and pressures can be extremely high, and as a consequence, the size scale of individual H II region complexes can be extremely small in comparison to the overall scale of the starburst. It is only when the star-forming complexes join up to produce large-scale collective phenomena as in, for example, the outflow in M82 that we need to go to a full three-dimensional radiative transfer model covering the whole galaxy.

In the earlier papers in this series, we take advantage of the localized radiative transfer approximation to construct our pan-spectral SEDs. Instead of treating the starburst as a single H II

region complex covering the whole starburst region, we split the starburst up into many individual H II regions, each ionized by the ultraviolet (UV) photons of the clusters within them and each evolving in radius and internal pressure according to the mechanical energy input of the exciting stars through their stellar winds and supernova explosions. The global SED is then the sum of the SEDs produced by each of these H II regions and their surrounding photodissociation regions (PDRs) integrated over all cluster ages. Since the radiative transfer problem in each H II region is fully treated, in this approach we stand a better chance of capturing the full range of physical conditions encountered in a starburst region. This collective approach is what can be found in many of the sophisticated modeling codes such as that of Piovani et al. (2006a) and GRASIL (Silva et al. 1998). In GRASIL, for example, multiple core molecular cloud systems can be included with differing parameters for each, such as mass and optical depth.

In the first paper (Dopita et al. (2005), we investigated the role that pressure alone plays in changing the compactness of the H II regions within the starburst and, hence, in the controlling the shape of the far-IR dust emission bump. However, a defect in these models is that they were only run with a single value of mean cluster mass $\langle M_{cl} \rangle$. A change in cluster mass directly affects the specific intensity of the radiation field in the H II region, and this will in turn change the shape of the far-IR bump.

In the second and third papers (Dopita et al. (2006b, 2006c), we introduced the $\mathcal{R} = \langle M_{cl} \rangle / P_0$ parameter, which controls the absolute value of the ionization parameter in the H II region and its time evolution. The ionization parameter is defined as the ratio of the ionizing photon density to the particle density in the H II region; $\mathcal{U} = L_{UV} / 4\pi R_{HII}^2 n c$, where L_{UV} is the flux of ionizing UV photons produced by the central cluster, R_{HII} is the mean radius of the H II region with particle density n , and c is the speed of light. All models having a given value of \mathcal{R} and metallicity Z will show the same run of ionization parameter as a function of cluster age and will therefore produce identical line ratios at any given age.

The shape of the dust feature or ‘‘bump’’ in the IR in starbursts is controlled by the distribution of dust temperatures in the starburst galaxy. Within a given H II region, this distribution of temperatures is controlled by the specific photon density, meaning that the mean dust temperature of any individual grain is $\langle T_{gr} \rangle = f(L_{UV}/R_{HII}^2)$. Thus, denser and more compact H II regions will produce hotter grain temperature distributions. In this paper, we introduce, by analogy with the \mathcal{R} parameter, a ‘‘compactness parameter,’’ \mathcal{C} . All models having a given value of \mathcal{C} and metallicity Z will show the same run of grain temperature distribution as a function of cluster age and will therefore produce identical far-IR dust reemission bumps at any given age.

In the following sections of this paper, we discuss the details of our modeling procedure, insofar as this is different from that used in earlier papers in this series, introduce the compactness parameter, and show that this does indeed serve to characterize the far-IR bump for H II regions in the age range 0.5–10 Myr. We also investigate the effects of varying metallicity on the form of the far-IR bump and provide templates for the mean SED of compact H II regions, of the older (10–100 Myr) stars, and for the attenuation produced by a dusty fractal foreground screen. Finally, we show how these components can be combined to produce excellent fits to frequently-used starburst templates such as Arp 220 or NGC 6240.

2. MODELS

The starburst models calculated here follow the general form described in the previous papers of this series (Dopita et al. 2005,

2006a, 2006c, ; hereafter SED1, SED2, and SED3, respectively). However, apart from being updated to use the latest versions of the modeling codes Starburst99 (Leitherer et al. 1999) and MAPPINGS III (Groves 2004), the models incorporate a number of changes or improvements that we here describe in greater detail. To make this paper self-contained, we briefly recapitulate on the techniques used in the earlier papers of this series.

2.1. Stars and Stellar Clusters

We have used the latest version (2006) of Starburst99⁷ to compute the SED of clusters of stars of any given age. A detailed description of latest stellar atmospheres and stellar evolution physics used within the code are given in Smith et al. (2002) and Vázquez & Leitherer (2005).

In our Starburst99 models, we take an instantaneous burst of $M_{\text{cl}} = 10^6 M_{\odot}$, having a Kroupa (2002) broken power-law IMF between 0.1 and $120 M_{\odot}$. Within the code we use the standard combination of the Geneva and Padova tracks for the stellar evolution (Vázquez & Leitherer 2005), and these determine the total mechanical luminosity, L_{mech} . We use the theoretical “high-mass-loss” tracks for the treatment of the stellar wind. The supernova cutoff mass is $8 M_{\odot}$. However, since the H II region evolution is run up to only 10 Myr, the exact choice of this cutoff mass is unimportant to the modeling.

We output the stellar spectra at 0.01 Myr, 0.5 Myr, and then every 0.5 Myr after that up to an age of 10 Myr, by which effectively all of the ionizing photons have been emitted (see SED2). Note that the resolution of the starburst model is actually higher at 0.1 Myr, which provides the fine gridding needed to accurately track the mechanical energy input used in the computation of the evolution of the H II regions. For completeness, this model was also extended to 1 Gyr, with spectra computed at longer intervals for older stellar templates.

To determine the parameters for clusters of any given mass, we assume a simple scaling with cluster mass. Such a scaling should hold in starbursting regions where many clusters are forming, as here stochastic effects are generally small, and on average the IMF is well sampled throughout the mass range. However, as a number of authors have pointed out, several of whom are referenced in SED2, and most recently by Weidner & Kroupa (2006), such an assumption will not hold for low cluster masses.

2.2. H II Region Evolution

The H II regions are treated as one-dimensional mass-loss bubbles driven by the mechanical energy input of their stars and supernovae (Castor et al. 1975). Their equation of motion is given by (SED1),

$$\frac{d}{dt} \left[R \frac{d}{dt} (R^3 \dot{R}) \right] + \frac{9}{2} R^2 \dot{R}^3 = \frac{3L_{\text{mech}}(t)}{2\pi\rho_0}, \quad (1)$$

where the time-dependent mechanical luminosity, $L_{\text{mech}}(t)$, is determined from the Starburst99 output.

The pressure in the H II region with radius R , expanding in an ISM with density ρ_0 is then determined as

$$P = n_{\text{H II}} k T_e, \\ = \frac{7}{(3850\pi)^{2/5}} \left(\frac{250}{308\pi} \right)^{4/15} \left[\frac{L_{\text{mech}}(t)}{\rho_0} \right]^{2/3} \frac{\rho_0}{R^{4/3}(t)}, \quad (2)$$

⁷ See Web site at <http://www.stsci.edu/science/starburst99/>.

TABLE 1
SOLAR ABUNDANCE SET (Z_{\odot}) AND LOGARITHMIC DEPLETION FACTORS $\log(D)$ ADOPTED FOR EACH ELEMENT

Element	$\log(Z_{\odot})$	$\log(D)$
H.....	0.00	0.00
He.....	-1.01	0.00
C.....	-3.59	-0.52
N.....	-4.20	-0.22
O.....	-3.34	-0.22
Ne.....	-3.91	0.00
Na.....	-5.75	-0.60
Mg.....	-4.42	-0.70
Al.....	-5.61	-1.70
Si.....	-4.49	-1.00
S.....	-4.79	-0.22
Cl.....	-6.40	-0.30
Ar.....	-5.44	0.00
Ca.....	-5.64	-2.52
Fe.....	-4.55	-2.00
Ni.....	-5.68	-1.40

where $n_{\text{H II}}$ is the density in the ionized gas, with electron temperature T_e . This equation is derived from the (Oey & Clarke 1997, 1998) version of the Castor et al. (1975) mass-loss bubble formulae with the assumption that the H II region has the same pressure as the shocked stellar wind and is confined to a thin shell around the periphery of the wind-blown bubble. The ionizing flux at the inner boundary of the H II region is then $L_{\text{UV}}/4\pi R^2$ and the density in the ionized region $n_{\text{H II}}$ is given by the first half of equation (2), from which the ionization parameter of the H II region, \mathcal{U} , can be derived.

2.3. Nebular Abundances and Depletion Factors

The abundance set and depletion factors used in these models are unchanged from those presented in SED3 and are given in Table 1. The nebular abundance set follows Asplund et al. (2005). As noted previously, the gas phase “Solar” abundance in the models is somewhat offset from the “Solar” abundance set used in Starburst99. While this has been shown to have no significant effect on the models, it does result in a small inconsistency in the models.

The exploration of metallicity effects within the models presented here is limited to those metallicities computed in Starburst99; 0.05, 0.2, 0.4, 1.0, and $2.0 Z_{\odot}$. As in SED3, we simply scale the abundances with metallicity, with the following exceptions. For helium we use the empirical relationship to include the primordial component as well as that from nucleosynthesis,

$$\text{He}/\text{H} = 0.0737 + 0.024(Z/Z_{\odot}). \quad (3)$$

The elements carbon and nitrogen are both observed to have a primary nucleosynthetic component and a secondary nucleosynthetic component at higher metallicities. Thus, for these elements we adopt the empirical relationships

$$\text{C}/\text{H} = 6.0 \times 10^{-5} (Z/Z_{\odot}) + 2.0 \times 10^{-4} (Z/Z_{\odot})^2, \quad (4)$$

$$\text{N}/\text{H} = 1.1 \times 10^{-5} (Z/Z_{\odot}) + 4.9 \times 10^{-5} (Z/Z_{\odot})^2. \quad (5)$$

The depletion factors used in the models are based on the observed depletion fractions in the local interstellar cloud (Kimura et al. 2003). These may not represent in reality those found in the starburst environments, but currently we have no adequate way

of estimating these. We must also assume that the depletion pattern does not vary with metallicity, as there are currently no good models or observations for the relationship between metallicity and depletion. However, in the starbursting environments modeled here, such an assumption may be adequate (Draine et al. 2007). With this assumption the dust-to-gas ratio is purely a function of metallicity.

2.4. Photoionization Models

For the component H II regions, we compute both the emission and internal absorption of both gas (line plus continuum) and dust (continuum including polycyclic aromatic hydrocarbons [PAHs]) using the MAPPINGS III code, with the Starburst99 stellar cluster spectra as input. Apart from the effects of burst age and metallicity, here we explore three other parameters within the models; the ISM pressure, P_0 , the cloud covering fraction, f_{PDR} , and the compactness parameter, C , described below, which is a function both of P_0 and of the mean cluster mass, $\langle M_{\text{cl}} \rangle$.

For the models investigated here we examine five different thermal gas pressures; $P_0/k = 10^4, 10^5, 10^6, 10^7$, and 10^8 K cm^{-3} . These five pressures cover the full range expected to be encountered in starbursting galaxies, from regions of enhanced star formation in disk galaxies, to the high-pressure ULIRGs. For each parameter set we compute models at 21 starburst ages, covering the timescale 0.01–10 Myr in steps of 0.5 Myr.

Finally, for each age we run two models. The first model is of the H II region alone; the region within which 99% of the hydrogen line emission arises and within which almost all of the ionizing photons are absorbed. It is within this region that the hottest dust emission arises. The second model corresponds to the PDR surrounding the H II region. This region is the transition layer between the H II region and surrounding dense molecular cloud, from which the stellar cluster is thought to have formed. In the PDR, a large fraction of the stellar light is absorbed and most of the PAH and dust far-IR emission produced. We follow the radiative transfer beyond the ionization front in the H II region until a total hydrogen column depth of $N(\text{H I}) = 10^{22} \text{ cm}^{-2}$ is achieved. The column depth of 10^{22} cm^{-2} is based on both observations and on theoretical considerations. The observational data come from measurements of individual molecular clouds both within our galaxy (Larson 1981; Solomon et al. 1987; Heyer et al. 2001) and in neighboring galaxies such as M33 (Rosolowsky et al. 2003) which all give hydrogen column densities of $\sim 10^{22} \text{ cm}^{-2}$ independent of cloud radius. This value is not unexpected, since it indicates that all giant molecular clouds are marginally stable against gravitational collapse, provided that their virial temperatures are a few tens of degrees kelvin.

These two models, H II and PDR, are combined through our final parameter, f_{PDR} , the starburst cloud covering fraction. This parameter is a simplified version of the clearing timescale introduced in SED1, and discussed in other dust models (e.g., Silva et al. 1998; Charlot & Fall 2000). We introduce this parameter because a starbursting system will be a conglomerate of bursts of different ages and sizes, unlike a single molecular cloud around an individual cluster. Thus, while the molecular cloud clearing timescale offers a more physical picture for an individual cluster, the starburst cloud covering fraction better represents what is likely to be encountered in a starbursting system.

The multiple star clusters forming in a starburst will be of all possible masses and, sampled at any instant in time, of all possible ages. To account for this we compute the luminosity-weighted average of all 21 ages computed between 0–10 Myr. In Figure 1 we show the SEDs of the 21 calculated ages of an individual H II region and a H II region with its PDR, along with the summed

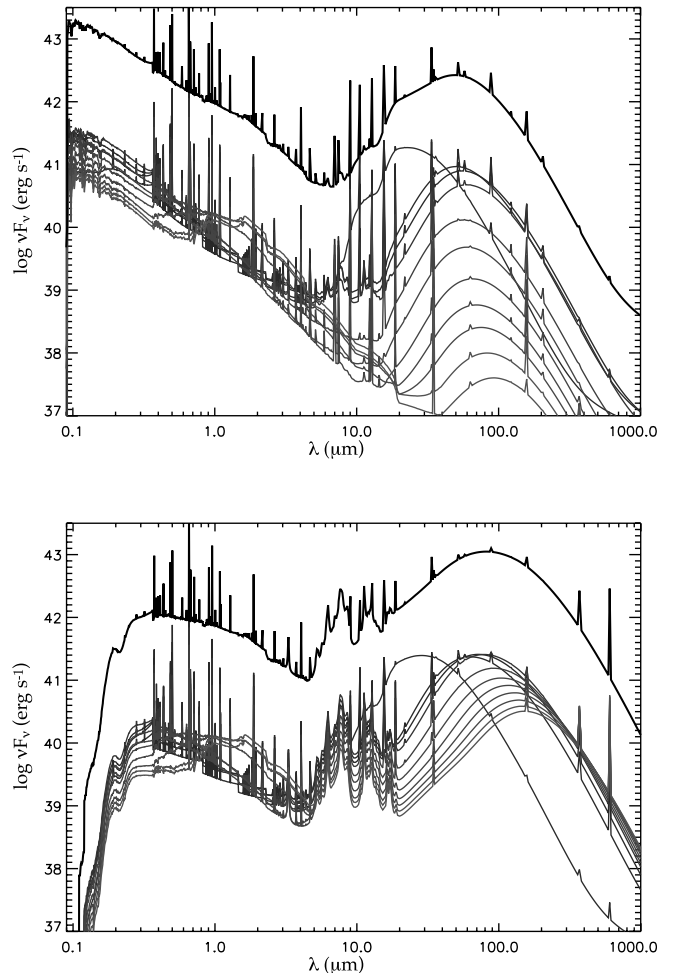


FIG. 1.—Evolution of the SED with age (0–10 Myr, every 1 Myr) for a $Z = 1 Z_{\odot}$, $\log C = 5.0$ ($\log \langle M_{\text{cl}} \rangle = 5$), $\log P/k = 5.0 \text{ K cm}^{-3}$ H II region-only model (top) and H II region plus PDR model (bottom). In both diagrams, the final, integrated starburst SED is shown as the thick line at high luminosity. [See the electronic edition of the Supplement for a color version of this figure.]

final average SED for each. These figures clearly show the evolution of both the stellar and nebular spectrum with age, and reveal the decreasing cluster UV flux and cooling dust temperatures as the clusters age and the H II bubble expands.

In all, we have computed a total 300 starburst H II region models covering five metallicities, six values of the C parameter (described below), five values of the ISM pressure, and a separate H II region and H II region plus PDR model for each set of parameters (corresponding to $f_{\text{PDR}} = 0$ and 1, respectively). All models are scaled in flux to correspond to a SFR of $1 M_{\odot} \text{ s}^{-1}$ continued over the 10 Myr lifetime of the H II regions.

2.5. Dust Physics

The treatment of dust within the photoionization code MAPPINGS III was discussed in SED1. Here, we concentrate only those areas where changes have been made to the dust parameters within the code.

In brief, our dust model consists of three components: graphites, silicates, and PAHs. The optical data for each of these come from Laor & Draine (1993), Li & Draine (2001), and Weingartner & Draine (2001)⁸ The IR spectrum arising from dust, excluding the effects of PAH emission, is calculated self-consistently, including

⁸ See Web site at <http://www.astro.princeton.edu/~draine/dust/dust.diel.html>.

the effects of stochastic heating in small grains (all dust calculations are discussed in detail in Groves [2004]). The total dust-to-gas ratio within the code is set by the fraction of metals depleted from the gas onto dust, given in Table 1.

The heavy elements removed from the gas phase are distributed between the two main types of dust, carbonaceous and siliceous, with the carbonaceous dust being further divided into graphite and PAHs. The graphite and silicate dust is distributed across a grain size distribution arising from grain destruction processes (SED1);

$$dN(a)/da = ka^{-3.3} \frac{e^{-(a/a_{\min})^{-3}}}{1 + e^{(a/a_{\max})^3}}, \quad (6)$$

with k defined by the dust-to-gas ratio. The minimum grain size of graphite and silicates are $a_{\min} = 20$ and 40 \AA , respectively, while the maximum grain size is the same for both species at $a_{\max} = 1600 \text{ \AA}$.

2.6. PAHs

PAHs are treated somewhat separately to the other types of dust. They are given a characteristic size and an opacity similar to coronene, the best-studied catacondensed PAH. We have constructed an empirically based IR emission spectrum described in more detail below. The PAH-to-gas ratio is defined through the PAH-to-carbon dust ratio, which is set at 30% in these models. While this may not be accurate for all environments and metallicities (Draine et al. 2007), it provides a reasonable match to current observations of nearby star-forming galaxies. Differences between the template IR emission spectrum and those actually observed will provide limits on parameters such as dehydrogenation, the relative abundance of catacondensed and pericondensed species, and the degree of nitrogen substitution within the carbon skeleton, which affects the $6.2 \mu\text{m}$ C—C stretch feature (Peeters 2002).

There is now a great deal of observational evidence that PAHs are destroyed within the ionized parts of the H II region complexes, with *Spitzer* observations of Galactic H II regions showing clear boundaries between the outer PDR PAH-emitting zone and the inner photoionized zone (e.g., Churchwell et al. 2006; Povich et al. 2007). The exact destruction mechanism is uncertain, but is likely to be photodestruction through stochastic heating and/or photoionization and dissociation. To simulate this process within the MAPPINGS III code, we previously introduced the Habing photodissociation parameter, $\mathcal{H} = F_{\text{FUV}}/n_{\text{HC}}$, a far-UV (FUV) analogy of the standard dimensionless ionization parameter \mathcal{U} (see eq. [17] and associated section in SED1). In a series of test models, we found that for typical, solar metallicity starbursts, $\mathcal{H} \sim 10^{-3}$ at the ionization front. We hereafter assume this value to be the destruction point for PAHs within our models. For typical H II densities of $10\text{--}100 \text{ cm}^{-3}$, this implies a radiation field $\sim 2\text{--}20$ times the Habing (1968) local interstellar radiation field, consistent with the range up to which PAHs are observed to survive (Compiègne et al. 2007). At values of $\mathcal{H} < 10^{-3}$, PAHs exist in either neutral or singly charged states, are heated by the diffuse FUV/optical field, and emit in the classic PAH mid-IR bands.

This emission spectrum is determined by the natural modes of vibration, bending, and other deformations of the planar carbon skeleton. This spectrum is dependent on the size and the electric charge state of the molecule, and is modified by the effect of non-hydrogenic end groups, including simple dehydrogenation and skeletal atomic substitution (Peeters 2002).

Thanks to the advent of space-borne IR observatories, the PAH emission spectrum has now been observed in many galaxies and situations, ranging from beautiful maps of Galactic H II regions

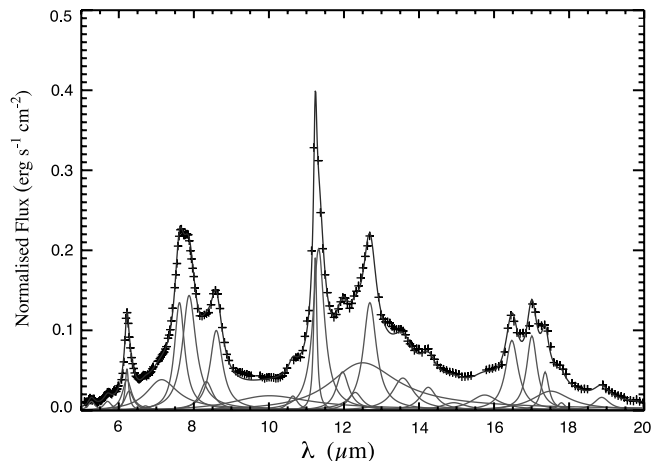


FIG. 2.—PAH emission template. Crosses indicate the observed points, with the solid line indicating our template fit, and the underlying curves showing the individual Lorentzian components. [See the electronic edition of the Supplement for a color version of this figure.]

(Churchwell et al. 2006) to detailed mapping of the features in both starburst galaxies (Beirão et al. 2007) and QSOs (Schweitzer et al. 2006).

Given the wide ranges of possible molecular forms, it is surprising that the form of the PAH emission spectrum in the mid-IR is so similar between different regions and galaxies (Brandl et al. 2006). Only small variations in the relative strengths of the PAH features have been observed within our own Galaxy and in nearby galaxies (Smith et al. 2007).

The accuracy of using a PAH template to represent the series of bands in the mid-IR can be estimated from the study of the variation of these bands in nearby galaxies by Smith et al. (2007). They find on average variations of a factor of 2 around the mean ratios of the different PAH bands (their Table 7), with the most significant differences occurring in galaxies hosting weak active galactic nuclei (AGNs; such as LINERs). This suggests that our PAH template is accurate to about this factor, with significant variations indicating differences such as PAH ionization state, or correspondingly, the presence of a weak AGN in the starburst galaxy. The differences between our models and the observed PAH bands could therefore be used as diagnostics of ISM physics or host nuclear properties.

As discussed in SED1, we parameterize the template using a sum of Lorentzian profiles. The Lorentzian fits to the spectrum take the form

$$F_{\nu}(x) = \frac{f_0}{\left[1 + (x - x_0)^2/\sigma^2\right]}, \quad (7)$$

where $x = 1/\lambda \text{ cm}^{-1}$, the central wavenumber of the feature is x_0 , the FWHM is 2σ , and the peak value is f_0 ($\text{ergs cm}^{-2} \text{ s}^{-1} \text{ Hz}^{-1} \text{ sr}^{-1}$).

To derive the PAH emission spectrum template currently used in these MAPPINGS III models, we have fit *Spitzer* IRS observations of NGC 4676 and NGC 7252. These two interacting galaxy pairs show strong, clear PAH emission, making them good choices for a template spectrum. In both objects we subtract the underlying dust continuum assuming a combined power law and exponential form to fit the PAH-free, long-wavelength end of the spectra. The combined, continuum-subtracted observed spectrum is shown with our best-fitting template in Figure 2. The

TABLE 2
NORMALIZED PARAMETERS OF THE LORENTZIAN
COMPONENTS OF THE PAH EMISSION BAND

x_0 (cm^{-1})	f_0 ($\text{ergs cm}^{-2} \text{ s}^{-1} \text{ Hz}^{-1} \text{ sr}^{-1}$)	σ (cm^{-1})
3040.3.....	1.006E-04	22.4
1897.0.....	1.000E-04	40.0
1754.0.....	1.000E-04	40.0
1608.5.....	3.420E-04	37.8
1608.5.....	4.600E-04	14.4
1593.9.....	2.140E-04	34.9
1490.0.....	5.000E-05	30.0
1400.0.....	3.420E-04	100.0
1313.0.....	1.200E-03	28.0
1270.0.....	1.280E-03	35.0
1200.0.....	3.200E-04	30.0
1163.1.....	8.900E-04	27.0
998.0.....	1.630E-04	129.1
940.0.....	1.600E-04	13.0
890.0.....	1.700E-03	4.0
883.0.....	1.800E-03	14.1
836.0.....	4.280E-04	14.1
813.0.....	2.000E-04	15.0
800.0.....	5.300E-04	70.7
788.0.....	1.200E-03	13.0
737.0.....	3.600E-04	18.2
702.0.....	2.570E-04	12.9
670.0.....	8.550E-05	18.3
635.0.....	1.710E-04	18.3
607.0.....	7.800E-04	7.5
588.0.....	8.300E-04	5.8
576.0.....	4.280E-04	4.0
571.0.....	2.140E-04	20.0
562.0.....	8.550E-05	3.8
530.0.....	1.450E-04	7.0

corresponding parameters for each of the Lorentzian profiles are given in Table 2.

As discussed in SED1, PAH emission within the MAPPINGS III code is treated as an energy-conserving process. In equilibrium all the energy gained by a PAH through the absorption of photons can be either lost through photoelectric processes or IR emission. Once the fraction of the energy lost through photoelectric processes is determined using the photoelectric cross-sections, the remaining energy fraction is reemitted in the IR according to our empirical template. This is not an exact treatment, as the PAH molecules will likely undergo stochastic heating processes and will lose some of their energy through IR continuum emission instead of *via* these fluorescent bands. However, the code does allow for the stochastic treatment of both very small graphite and silicate grains.

3. THE \mathcal{C} PARAMETER

We now deal with the parameter which controls predominantly the form of the far-IR continuum. Fundamentally, this continuum is a function of the probability distribution of the grain temperatures throughout the starburst. At any point within an H II region or its surrounding PDR, this is determined by the intensity and the SED of the stellar radiation field. Thus, at radius R in a spherical nebula for any individual grain species, s ,

$$\langle T_{\text{gr}}(s) \rangle = f(L_*/4\pi R^2, \bar{\nu}), \quad (8)$$

where $\bar{\nu}$ is the mean photon energy of the radiation field, which depends both on the age of the cluster and the solution of the

radiative transfer problem out to radius R . Thus, if we wish to find a variable in which H II region models evolve along a unique grain temperature distribution in time, $\langle T_{\text{gr}}(s, t) \rangle$, these models must also preserve the run of $L_*(t)/4\pi R(t)^2$. Then, because all models of this kind give a similar run of grain temperature distributions, they will also produce very similar global far-IR dust emission distributions. With a particular choice of cluster luminosity, physically denser H II region models have smaller radii and, hence, have hotter dust temperature distributions.

We therefore define a compactness parameter, \mathcal{C} , in the form

$$\mathcal{C} \propto \frac{\langle L_*(t) \rangle}{\langle R(t)^2 \rangle}. \quad (9)$$

This variable is akin to the compactness factor found in the models of Tagaki et al. (2003a, 2003b) in that it directly determines the dust grain temperature distribution. The ratio on the right is also comparable to the ratio $m_{\text{mc}}/r_{\text{mc}}^2$ discussed in Silva et al. (1998), which controls the SED of their molecular clouds, and therefore, the resulting hot dust SED of their models. The stellar luminosity $L_*(t)$ scales with the cluster mass M_{cl} , and the radius and pressure at any instant scale according to the simple mass-loss bubble approximation of (Castor et al. 1975)

$$R = \left(\frac{250}{308\pi} \right)^{1/5} L_{\text{mech}}^{1/5} \rho_0^{-1/5} t^{3/5}, \quad (10)$$

$$P = \frac{7}{(3850\pi)^{2/5}} L_{\text{mech}}^{2/5} \rho_0^{3/5} t^{-4/5}, \quad (11)$$

where L_{mech} is the instantaneous mechanical luminosity of the central stars of the burst (which can be assumed to scale as the mass of the cluster) and ρ_0 the density of the ambient medium. Note that the ambient number density is $n_0 = \rho_0/(\mu m_{\text{H}})$ and ambient pressure $P_0 = n_0 k T_0$.

From these equations it follows that

$$\mathcal{C} \propto \frac{\langle L_*(t) \rangle}{\langle R(t)^2 \rangle} \propto \frac{L_*}{L_{\text{mech}}^{2/5} P_0^{-2/5}} \propto M_{\text{cl}}^{3/5} P_0^{2/5}. \quad (12)$$

This product remains to be normalized. By analogy with the \mathcal{R} parameter introduced in SED3, we choose to adopt as the normalized definition of the compactness parameter

$$\log \mathcal{C} = \frac{3}{5} \log \left(\frac{M_{\text{cl}}}{M_{\odot}} \right) + \frac{2}{5} \log \left(\frac{P_0/k}{\text{cm}^{-3} \text{ K}} \right), \quad (13)$$

where M_{cl} should now be understood as the mean (luminosity-weighted) cluster mass in the starburst. The likely allowable physical range on $\log \mathcal{C}$ in starburst environments is, roughly, 3–7.5. These extremes correspond to $\log[(P/k)/\text{cm}^{-3} \text{ K}] \sim 4$ and $\log(M_{\text{cl}}/M_{\odot}) \sim 3.5$ and $\log[(P/k)/\text{cm}^{-3} \text{ K}] \sim 8$ and $\log(M_{\text{cl}}/M_{\odot}) \sim 7$, respectively.

In Figure 3 we show the variation of L_*/R_{HII}^2 with time for six different \mathcal{C} parameters. These display a strong decrease of the incident flux and, therefore, of dust temperature with time. The specific flux changes several orders of magnitude over 10 Myr. This decrease is due to both the increase of the H II bubble radius with time (see Fig. 1 in SED1), and the decreasing cluster luminosity as the higher mass stars die out. Note that because of the underlying power-law behavior of \mathcal{C} , on this log scale the curves for different \mathcal{C} parameters are offset from each other in proportion to the change in $\log \mathcal{C}$.

In order to demonstrate the constancy of the dust temperature distribution at constant $\log \mathcal{C}$, in Figure 4 we show overplotted

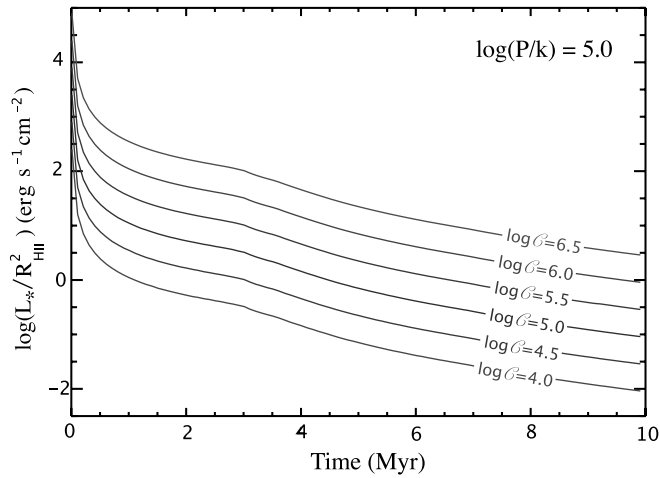


FIG. 3.—Time variation of the incident heating flux ($L_*/R_{\text{H II}}^2$) entering the H II region surrounding a solar metallicity starburst with $\log(P_0/k) = 5$. Each curve represents a different C (M_{cl}), and reveals how the C parameterizes different $L_*/R_{\text{H II}}^2$ at any given time. [See the electronic edition of the Supplement for a color version of this figure.]

five SEDs for Solar metallicity PDRs, which all have the same compactness parameter of $\log C = 5.0$, but which have different pressures and stellar cluster masses. Although these five SEDs appear indistinguishable, they are not exactly the same, because their nebular excitation parameters (\mathcal{R} ; see SED3) are quite different, and consequently, their nebular continuum and emission lines are different.

Provided that we could independently determine \mathcal{R} (from the nebular spectrum) and C (from the form of the dust continuum), then in principle we could solve independently for the mean pressure, P_0/k , and mean cluster mass, M_{cl} :

$$\log\left(\frac{M_{\text{cl}}}{M_{\odot}}\right) = \log C + \frac{2}{5} \log \mathcal{R}, \quad (14)$$

$$\log\left(\frac{P_0/k}{\text{cm}^{-3} \text{K}}\right) = \log C - \frac{3}{5} \log \mathcal{R}. \quad (15)$$

In practice, the separation of these variables would be assisted by a direct measurement of the gas pressure. For $P_0/k > 10^6 \text{ cm}^{-3} \text{ K}$

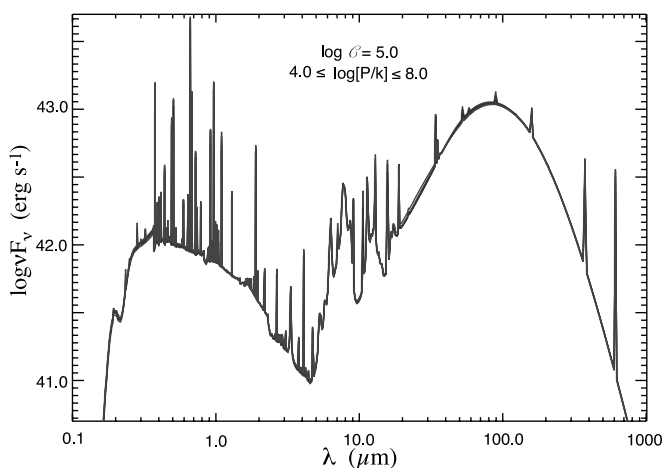


FIG. 4.—Five SEDs with Solar metallicity, $\log C = 5.0$, and varying pressure ($\log P/k = 4, 5, 6, 7$, and 8). The model SEDs are almost indistinguishable apart from their nebula emission features, such as the [Ne II] $12.8 \mu\text{m}$ emission line. [See the electronic edition of the Supplement for a color version of this figure.]

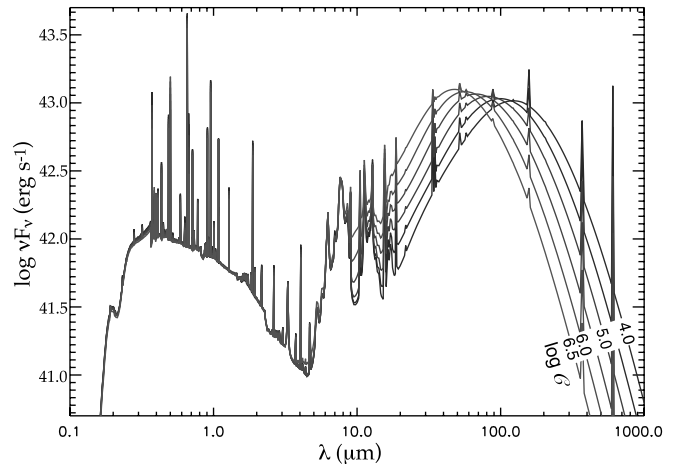


FIG. 5.—Six model SEDs with Solar metallicity, $\log P_0/k = 5.0$, and varying compactness. The compactness parameter decreases from $\log C = 6.5$ to $\log C = 4.0$ as the far-IR dust emission feature moves to longer wavelengths. [See the electronic edition of the Supplement for a color version of this figure.]

we can use the ratio of the [S II] $\lambda 6717, 6731$ lines for this purpose.

To show the effect of varying C on the form of the far-IR SED, we present in Figure 5 six model PDR SEDs having the same metallicity ($1 Z_{\odot}$) and pressure ($P/k = 10^5$), with C varied by varying the cluster mass. In the optical and near-IR, the model SEDs show stellar emission, and the extinction of all six SEDs is the same, as they pass through the same column depth of dust and gas. At longer wavelengths, the progression in the dust temperatures with increasing C is obvious.

4. PDR COVERING FRACTION

In § 3, our Figures 4 and 5 corresponded to a complete covering fraction of molecular clouds; $f_{\text{PDR}} = 1$. In this extreme, the molecular gas and dust surrounding the H II regions act as a dust bolometer, absorbing essentially all of the stellar UV continuum, and reradiating it into the far-IR bump and the PAH features. However, in the case of isolated H II region complexes in both starburst and in normal disk galaxies, the placental molecular cloud is quickly cleared away by the stellar winds, and by photoevaporation. In older clusters, the disruption of the cluster by this gas ejection will cause the exciting stars to disperse away from the regions of high extinction, although the timescale for this may be greater than the H II region lifetime (Boily & Kroupa 2003a, 2003b). This process is cutely referred to as “infant mortality.”

Previously in SED1 and SED2, we parameterized this uncovering of the exciting stars by the introduction of a molecular cloud clearing or dissipation timescale, τ_{clear} , where the covering fraction of molecular cloud PDRs around a stellar cluster is given by;

$$f_{\text{PDR}} = \exp(-t/\tau_{\text{clear}}). \quad (16)$$

In SED2, we found that, for Galactic star-forming regions at least, this timescale is quite short, on the order of 1–2 Myr. However, this certainly does not represent all star-forming regions and is probably far too short for ULIRGs which have an extremely generous sink of molecular material. In these objects, the H II regions of individual clusters may merge, but the complex is still surrounded by molecular gas. Thus, the clearing timescale is likely to show a large range and will depend on the local environment. In addition, situations like the commonly observed “blister H II

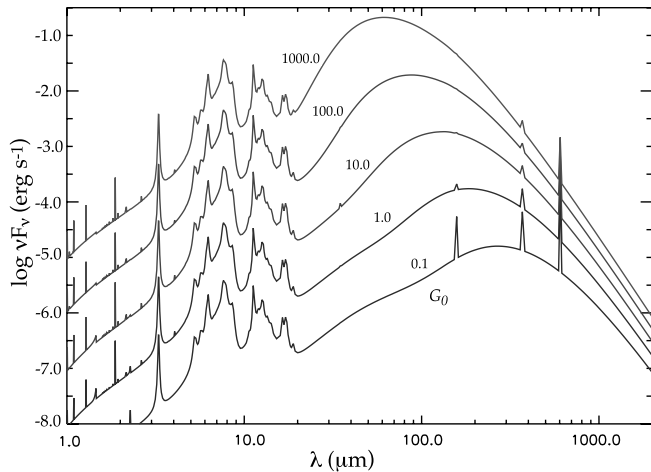


FIG. 14.—Cool dust emission for a Habing radiation field density, G_0 , of 0.1, 1.0, 10.0, and 100.0 times the local ISRF density of Habing (1968). The strength of the radiation field increases from bottom to top. [See the electronic edition of the Supplement for a color version of this figure.]

the surrounding molecular gas. Note also that at the highest A_V even the 20–35 μm slope steepens to the “reddening” effect of the dust attenuation.

The $A_V > 20$ mag dusty screen needed to provide the observed depth of the silicate absorption troughs seen in some ULIRGs has little effect on the global energy balance of the starburst. By an A_V of 1.0, most of the FUV–optical radiation from stars, almost 80%, has been absorbed (or scattered) by dust. The decline in the luminous flux through the PDR, accompanied with the softening of the radiation field naturally produces the dust temperature gradient which Levenson et al. (2007) believe is required in the obscuring material.

6.4. Diffuse Dust Emission and Scattering

A complete model of a starburst environment should not neglect the contribution to the far-IR emission by diffuse cool dust. Some of this may well be the same dust that produces the foreground screen absorption. The optical photons that are absorbed by the diffuse galactic dust at high A_V are still capable of heating the dust in the diffuse ISM. In addition, the star-forming regions may not be fully cocooned by its surrounding PDR cloud, so that some fraction of the cluster UV radiation may escape and heat this diffuse dust. This cool galactic dust will mostly contribute to the SED in the $>100 \mu\text{m}$ to submillimeter region. A portion of this radiation may also be scattered into our sight line, which mostly affects the far-UV SED. In our modeling we have not included this component due to our limited geometry.

The exact temperature distribution of the grains will also depend on the geometry of the starburst, preexisting stellar population, and dust within the starbursting galaxy. Because of the limited geometry of our simple models, we are unable to model such distributions. Instead we follow the work of Dale et al. (2001) and calculate the diffuse cool dust emission in terms of the average interstellar radiation density. This allows us to model both distributed starbursts where the average radiation field is high, and nuclear starbursts, where the rest of the galactic scale dust is only weakly heated.

To represent the average radiation field we have used the luminosity weighted average of a Starburst99 cluster from 10–100 Myr discussed in the § 6.2. While this is younger than the average age of the preexisting stars in a starburst host galaxy, these stars are

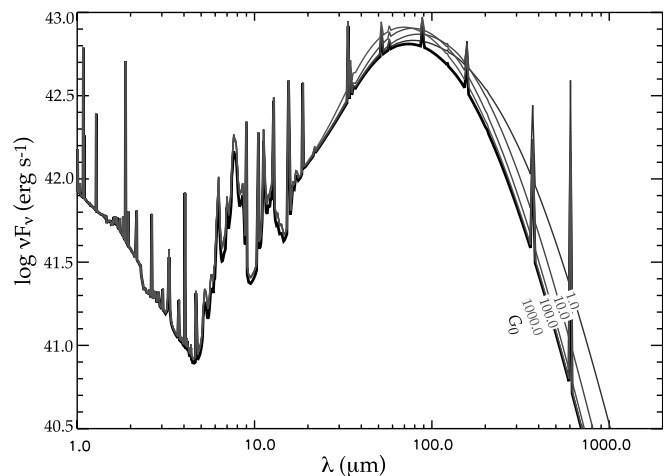


FIG. 15.—Five SEDs demonstrating the effect of adding diffuse dust emission at 10% of the starburst luminosity to our fiducial model starburst ($1 Z_\odot$, $\log C = 5$, $\log P/k = 5$, and $f_{\text{PDR}} = 0.5$). The SEDs show the original SED (thick line) and those with an added diffuse dust continuum heated by a young stellar continuum 100.0, 10.0, 1.0, and 0.1 times that of the local ISRF. [See the electronic edition of the Supplement for a color version of this figure.]

nonetheless likely to provide the dominant dust-heating radiation field.

We then calculate the cool dust emission using the MAPPINGS III code, assuming the same dust properties as before and a column depth of $\log N(H) = 22.5 \text{ (cm}^{-2}\text{)}$. For the heating flux we scale the radiation field in terms of the local Habing (1968) interstellar radiation field (ISRF: $\text{FUV} \sim 1.6 \times 10^{-3} \text{ ergs s}^{-1} \text{ cm}^{-2}$). We set the radiation field from 0.1 to 1000.0 times this value, in steps of 0.3 dex. The resulting IR emission is shown in Figure 14. As expected, low ISRF leads to very cold dust, and the high ISRF has dust temperatures similar to those encountered in our PDRs.

The actual contribution of this diffuse dust emission component to the global starburst SED is not constrained by these models. This would require a more sophisticated geometrical model of the starburst, its outflows, and any more extended disk or tidal structure around the starburst core.

In Figure 15 we show the effect of adding this diffuse dust emission component with a total intensity of 10% of our fiducial model starburst with solar metallicity. For clarity we add only four of the diffuse emission models, heated by a Habing radiation field, G_0 of 1000.0, 100.0, 10.0, and 1.0 times the local ISRF ($\text{ISRF}_{\text{local}}$), respectively. The attenuation associated with the diffuse dust emission is not included here.

The model with 1000.0 times $\text{ISRF}_{\text{local}}$ has hotter dust than the $\log C = 5$ PDR and is therefore likely to be unphysical. The 100.0 times $\text{ISRF}_{\text{local}}$ model has a similar dust temperature as the PDRs, and so the diffuse field serves only to increase the total flux of the IR. This probably represents the extreme case for a starbursting galaxy, and may lead to the narrow and strong FIR features seen in some ULIRGs.

The cooler diffuse emission models, with $G_0 < 10.0$ times $\text{ISRF}_{\text{local}}$, are both applicable to less energetic starburst galaxies. In such cases, the diffuse emission acts to broaden the IR feature, as well as shift the peak to longer wavelengths, while leaving the shorter wavelengths ($<60 \mu\text{m}$) relatively unaffected.

7. STARBURST METALLICITY

The metallicity of a starburst affects the SED in several ways; through the intrinsic change in the stellar SED with metallicity,

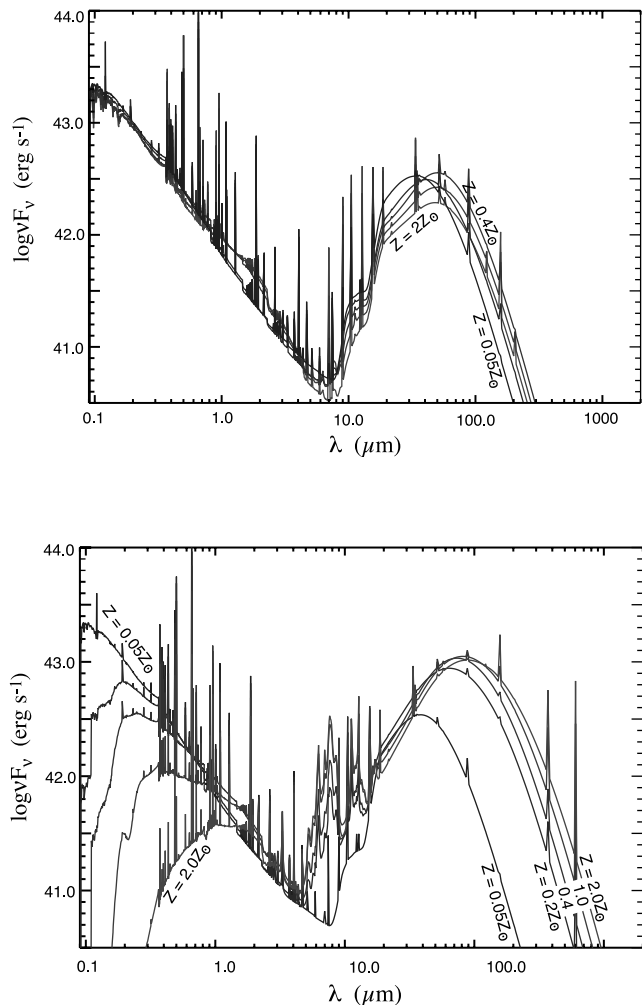


FIG. 16.—Effects of changing metallicity on the H II region spectra (top) and PDR spectra (bottom) of a $\log C = 5$, $\log P_0/k = 5$ starburst. [See the electronic edition of the Supplement for a color version of this figure.]

through the changing gas-phase abundances, which determine the temperature and the line emission of the H II regions, through the opacity of the ISM in the dust, and through the metallicity-dependent change in grain composition. A full discussion of the effect of metallicity on the emission-line spectra of the H II regions was given in SED3. In this section we systematically investigate the remaining effects.

In Figure 16 we show our fiducial (H II region and PDR) starburst with $\log C = 5$ and $\log P_0/k = 5$ computed using the five standard Starburst99 metallicities. As the PDR is defined through a constant column depth of hydrogen, lower metallicity leads to lower column of dust. This leads to a strong decrease in the optical-ultraviolet opacity as the metallicity is decreased.

The metallicity-dependent effects on the H II emission-line spectrum have previously been remarked on in SED3. As the metallicity decreases, the stellar spectrum becomes harder due to the decreasing opacity of the stellar atmospheres and winds. In addition, for a given size, a stellar cluster of lower metallicity has a higher ionizing luminosity and lower mechanical luminosity. This leads to more compact H II regions, and higher ionization parameters in the surrounding H II region. The fraction of radiation absorbed by the dust in the H II region depends on the product of metallicity and ionization parameter (Dopita et al. 2003). This product remains approximately constant with metallicity,

ensuring that the flux under the far-IR bump remains approximately constant for the H II region SEDs.

In the PDRs, the UV to optical SEDs clearly show the effect of increasing opacity with metallicity. The far-IR features change in several ways. First, there is a systematic increase in the relative strength of the PAH emission features with metallicity. This is a consequence of the increase in the C/O ratio with metallicity, which ensures that PAHs account for more absorption at higher metallicity relative to the silicates, combined with the higher mean dust temperatures which characterize lower metallicities. Another factor is the increased strength and hardness of the average radiation field in the constant column PDR with decreased metallicity. As a consequence, the Habing PAH survival criterion is only met deeper in the cloud, resulting in overall weaker PAH emission.

Such a decrease in the PAH strength with decreasing metallicity has been observed with both *Spitzer* and *ISO* (Engelbracht et al. 2005; Rosenberg et al. 2006; Wu et al. 2006; Madden et al. 2006; Jackson et al. 2006). However, the observed depletion of PAHs in the low-metallicity environments may be even greater than that computed in our models, and both Wu et al. (2006) and Jackson et al. (2006) implicate grain destruction processes as acting more efficiently in the lower metallicity environments. We would hope that our models, applied to these low-metallicity systems, would be able to better confirm and quantify this effect.

In the PDRs, the IR flux can also be seen to increase and become broader with metallicity up until $Z \sim 1.0 Z_\odot$, after which it stays approximately constant. This is predominantly due to the increased dust column. The shift of the IR peak to longer wavelengths is also partly due to the increased dust column but is also due to the increasing mechanical luminosity of the starburst with metallicity, which results in larger H II regions, with cooler average dust temperatures.

8. COMPARISON WITH OBSERVATIONS

8.1. Data Sources

In order to compare the models with data, we require as close a homogeneous data set as available, covering as wide a wavelength range as possible. For this purpose, we have selected a pair of popular template starburst galaxies, NGC 6240 and Arp 220 from the 41 ULIRGs observed with *ISO* by Klaas et al. (2001). This data set is ideal for our purpose because their SEDs are well sampled over the full wavelength regime 1–200 μm .

Flux densities at other wavelengths were collected using the NASA/IPAC Extragalactic Database (NED) supplemented with a wide selection of online catalogs and papers. Generally, the UV/optical fluxes are taken from the *Third Reference Catalog of Bright Galaxies*, version 3.9 (de Vaucouleurs et al. 1991). Many optical and near-IR fluxes were taken from Spinoglio et al. (1995) or from the APM and 2MASS databases.

The majority of data points in the 1–1300 μm wavelength range come from Klaas et al. (1997, 2001). Additional data points were taken from Sanders et al. (1988a, 1988b), Murphy et al. (1996), Rigopoulou et al. (1996, 1999), Surace & Sanders (2000), Lisenfeld et al. (2000), Dunne et al. (2000), Dunne & Eales (2001), Scoville et al. (2000), and Spoon et al. (2004) and references therein.

When available, the UV/optical and near-IR (*JHK*-band) points include aperture corrections to allow a direct comparison with the larger aperture mid- and far-IR fluxes (see, for example, Spinoglio et al. 1995). All UV to near-IR fluxes have been corrected for Galactic extinction using the $E(B - V)$ values based on *IRAS* 100 μm cirrus emission maps (Schlegel et al. 1998) and extrapolating following Cardelli et al. (1989).

For comparison of the models with a typical *Spitzer* IRS spectrum of a starburst, we have used the latest (recalibrated) version of the spectrum of NGC 7714 from Brandl et al. (2006).

8.2. Pan-Spectral Fitting

Our library of models contains the following elements:

1. An ensemble of H II regions surrounding young clusters with ages < 10 Myr characterized by mean compactness C and metallicity Z .
2. A set of PDRs surrounding these H II regions with a mean geometrical covering factor, f_{PDR} .
3. A population of young (< 1.0 Myr) UCHII regions and their PDRs surrounding individual massive stars, characterized by a fraction f_{UCHII} , where $f_{\text{UCHII}} = 1.0$ would imply that 50% of massive stars younger than 1.0 Myr were surrounded by UCHII regions.
4. An older stellar population with ages $10 \leq t \leq 100$ Myr. The flux of this component is scaled by a factor f_{old} , where $f_{\text{old}} = 1$ would correspond to continuous star formation over a total period of 100 Myr.
5. A foreground turbulent attenuating dust screen, characterized by an optical depth in the V band, A_V .
6. A reemission component from the diffuse ISM, characterized by the mean Habing field intensity G_0 and scaled to a percentage of the total bolometric flux of the starburst ($\leq 20\%$).

Ideally, all of these elements should be fitted via a nonlinear least-squares procedure. However, lacking this tool for the time being, we have elected to make handcrafted fits to a few template objects. In addition, we have chosen to make the following simplifying assumptions:

1. We treat the < 10 Myr stellar population as an ensemble of H II + PDR regions with $f_{\text{PDR}} = 1.0$. This approximation is justified by the observation that the global obscuration of a starburst increases with the absolute SFR (Buat et al. 1999; Adelberger & Steidel 2000; Dopita et al. 2002; Vijn et al. 2003). This is a natural consequence of the Kennicutt (1998) star formation law, connecting the surface density of star formation to the surface density of gas; $\Sigma_{\text{SFR}} \propto \Sigma_{\text{gas}}^n$, with $n \sim 1.3-1.6$. Noting that $A_V \propto \Sigma_{\text{gas}}$, it follows that intense starbursts are highly dust enshrouded.
2. We ignore the contribution of the diffuse dust in the far-IR emission. As has already been noted in § 6.3, the contribution this makes is small and significant only above $100 \mu\text{m}$.

With these assumptions, we show in Figure 17 the fit we obtain for the galaxy NGC 6240. As can be seen, with five free parameters we obtain an excellent fit to the observations over nearly 3.5 decades of frequency. In this figure, the data have been scaled to a SFR of $1.0 M_{\odot} \text{ yr}^{-1}$ in order to make this SED comparable to the others in this paper. The scaling factor required indicates a total SFR of $120 M_{\odot} \text{ yr}^{-1}$ for this galaxy, a little higher than the value of $102 M_{\odot} \text{ yr}^{-1}$ derived from the *IRAS* far-IR luminosity by Dopita et al. (2002). However, the $H\alpha$ luminosity for this galaxy (also measured by Dopita et al. 2002), which comes from the extended gas indicates a SFR of $14.6 M_{\odot} \text{ yr}^{-1}$, provided that it is dominated by star formation and not by an obscured active nucleus (see below). Since the far-IR comes from the obscured starburst and the visible $H\alpha$ from the regions which are relatively unobscured, these figures suggest that the total SFR is indeed close to $120 M_{\odot} \text{ yr}^{-1}$.

As can be seen in Figure 17, with a model with only five free parameters we have obtained an excellent fit to the observations over nearly 3.5 decades of frequency. However, this quality of fit to a model which only includes elements of a starburst system is

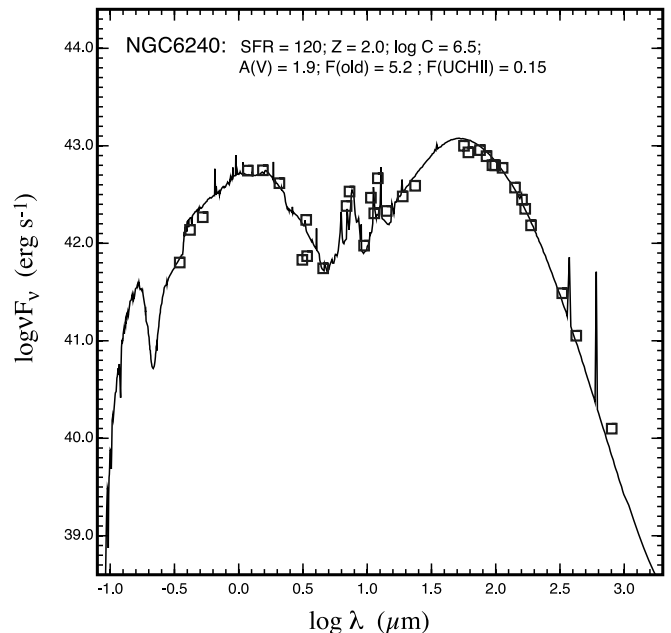


FIG. 17.—Fit to the starburst galaxy NGC 6240. The errors in the observed fluxes are similar in magnitude to the height of the blue squares. The parameters of the fit are given on the label. Note that although here A_V is estimated at 1.9 mag, this applies to the older stars. For the younger stars in the H II regions, $A_V \sim 4.4$ mag in this model. [See the electronic edition of the Supplement for a color version of this figure.]

at first sight extraordinary. NGC 6240 has long been implicated with an active nucleus and shows both a strong nonthermal radio excess, extended radio emission (Gallimore & Beswick 2004), and X-ray emission associated with a highly dust-obscured AGN (e.g., Ikebe et al. 2000; Risaliti et al. 2000; Kewley et al. 2000). Recently Armus et al. (2006) have directly detected the active nucleus via the $[\text{Ne v}]$ $14.3 \mu\text{m}$ line using the IRS on the *Spitzer Space Telescope*. From this, they estimate that the AGN has a flux of 3%–5% of the bolometric luminosity. At such low levels, it would account for the slight excess in the flux in the vicinity of the 6–14 μm PAH features seen in the observations when compared to our model, but is not sufficient to compromise the rest of the fit.

NGC 6240 has an unusually strong contribution from older stars, suggesting either that the starburst is rather old in this object, or that the current starburst is the second episode in this galaxy, or that there is an important contribution of stars older than $\sim 10^8$ yr. All of these hypotheses are consistent with the known status of NGC 6240 as a postmerger system.

What about the uniqueness of this fit? Fortunately, the different parameters of the fit act on different parts of the pan-spectral SED, so it is fairly easy to separate them when we have data covering such a large range in wavelength. We have performed the test of varying each of the major parameters, excluding metallicity, systematically around the best-fit solution, and the result is shown in Figure 18.

The effect of varying metallicity is shown in Figure 16, and has perhaps the most profound effect on the spectrum. To summarize, the metallicity is most easily determined from the shape and absorption-line intensities of the stellar continuum and by the emission-line techniques discussed in SED3. It also has an effect on both the strength of the PAH features and the width of the far-IR bump. High metallicity gives strong PAH features and wide far-IR bump. In the fitting described in this section we have mostly relied on these latter characteristics to estimate the abundance.

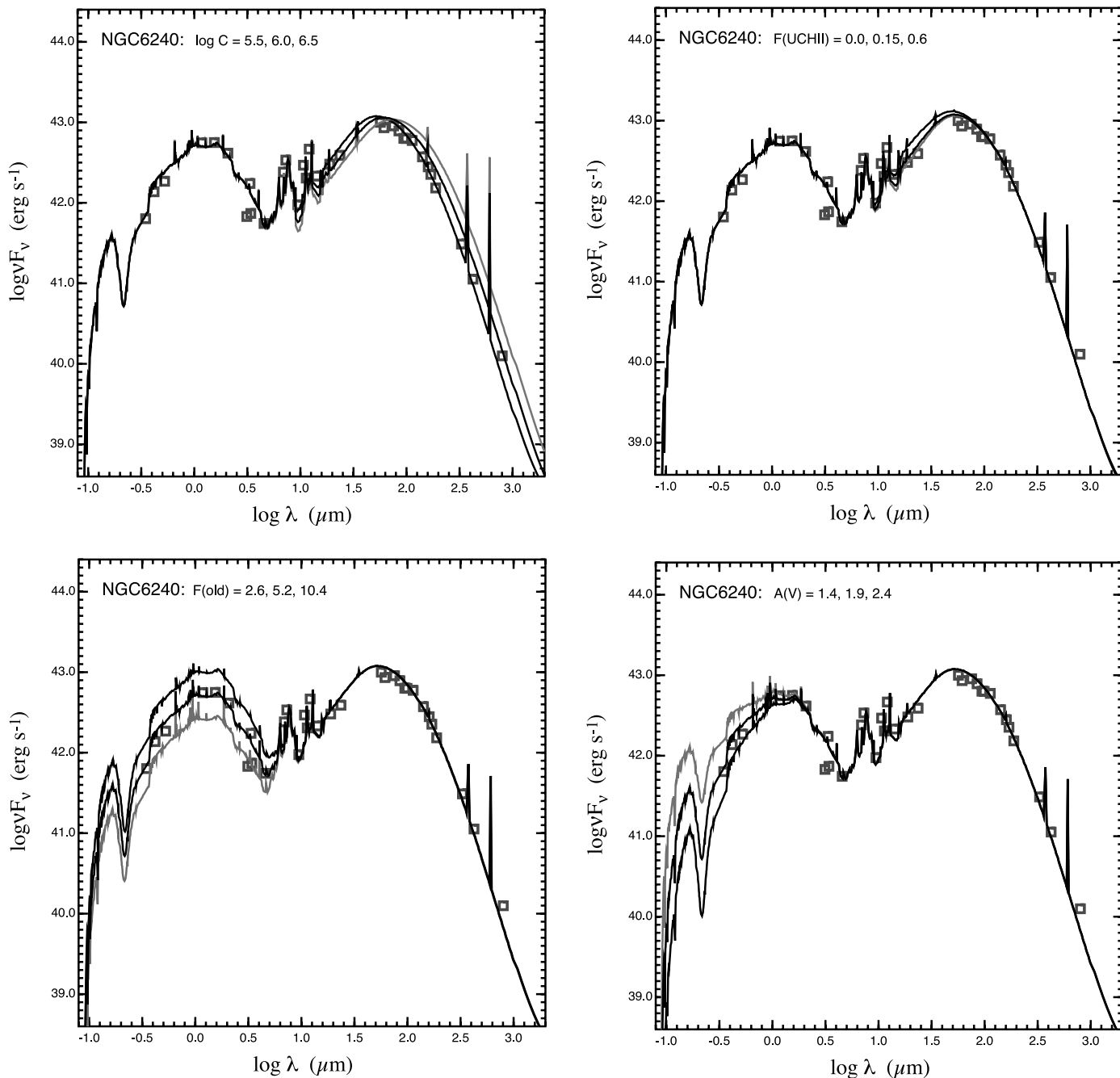


FIG. 18.—Sensitivity of fit to the starburst galaxy NGC 6240 to the various parameters. As can be seen, for this galaxy, $\log C$ is constrained within ± 0.25 dex, A_V to ± 0.3 mag, and f_{old} to within 20%. The fraction of UCHII regions, f_{UCHII} is not very well constrained in this galaxy, owing to its high compactness, but would be much better constrained in galaxies with $\log C < 5$. [See the electronic edition of the Supplement for a color version of this figure.]

For the remaining parameters, Figure 18 shows that each affects a different part of the SED. A change in $\log C$ only changes the far-IR bump, shifting it in peak wavelength without appreciable change in the total width. A change in f_{old} simply scales the $0.091\text{--}5\ \mu\text{m}$ spectrum up and down, leaving the rest of the SED unchanged. A change in A_V affects the slope of the visible-UV spectrum. Note that when A_V is higher than about 5–10 mag, the 9.7 and $18.0\ \mu\text{m}$ silicate absorption features appear and can be used to constrain the extinction when the visible-UV part of the spectrum is too attenuated. The UCHII region fraction f_{UCHII} mostly affects the $10\text{--}30\ \mu\text{m}$ part of the spectrum. In Figure 18, the apparent sensitivity of the SED to this parameter seems small, but this is because the inferred $\log C$ for this galaxy is very high.

Thus, the flux of the ordinary H II regions is high in the $10\text{--}100\ \mu\text{m}$ region where the UCHII population is important, and the contribution of the UCHII regions is veiled. Galaxies with lower $\log C$ show the UCHII contribution much more clearly (see Fig. 9).

As another example of a famous starburst, we present in Figure 19 our fit to Arp 220, the predominantly used template of starburst SEDs. This galaxy is characterized by a greater optical extinction, lower compactness parameter, and a lower contribution of the old star population than NGC 6240. In addition, a lower chemical abundance is indicated by the weaker PAH features, and the narrower, more sharply peaked far-IR bump.

Arp 220, as the local ULIRG, has quite often been used as a testbed for SED modeling. Examples of these can be seen in Silva

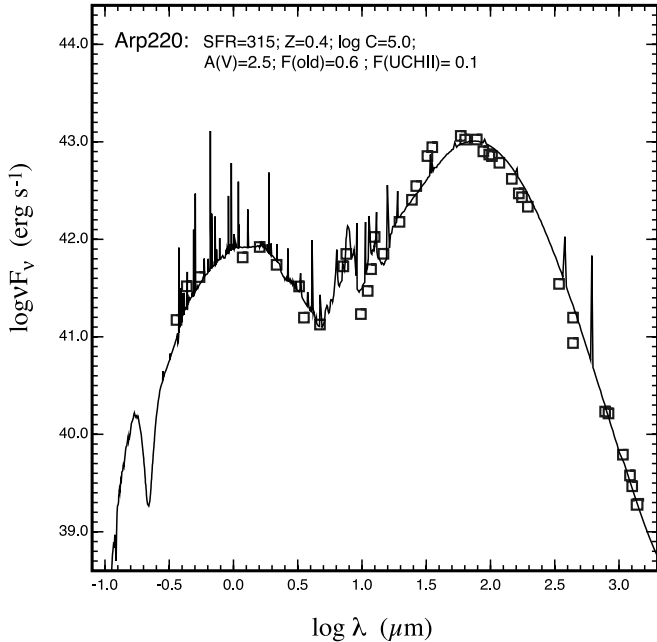


FIG. 19.—Standard fit to the starburst galaxy Arp 220. [See the electronic edition of the Supplement for a color version of this figure.]

et al. (1998, their Fig. 9), Tagaki et al. (2003b, their Fig. 8), and Siebenmorgen & Krügel (2007, their Fig. 5) to name a few. While all these models (including our own) can be seen to fit quite reasonably the available observations of Arp 220, they differ in their model parameters, making direct comparisons difficult. However the main physical conclusions drawn from the models are the same, and comparisons here can give insight into both the models and Arp 220 itself.

All models suggest a SFR for Arp 220 of $\sim 300 M_{\odot} \text{ yr}^{-1}$. We derive a SFR of $315 M_{\odot} \text{ yr}^{-1}$, which can be compared with the $270 M_{\odot} \text{ yr}^{-1}$ obtained by Shioya et al. (2001), $260 M_{\odot} \text{ yr}^{-1}$ from Tagaki et al. (2003a), and $580 M_{\odot} \text{ yr}^{-1}$ from Silva et al. (1998).

In connection with this is the total luminosity of Arp 220, which is $\log L_{*} = 12.16(L_{\odot})$ in our models, close to the value of 12.1 of Tagaki et al. (2003a) and Siebenmorgen & Krügel (2007) and just below the value of 12.4 from Silva et al. (1998). For the total stellar mass of Arp 220 we obtain $\log M_{*} \sim 10.5(M_{\odot})$, higher than the previous SED model estimates of 10.4 (Silva et al. 1998) and 10 (Tagaki et al. 2003a), but due to the low mass-to-light ratio of our older stellar component (§ 6.2), this value is somewhat uncertain. All these values indicate that both our model and fit to Arp 220 are at least consistent with previous models and suggest the true values for Arp 220.

One well-known detail of Arp 220 is its very high nuclear extinction; $A_V \sim 30$ (Shioya et al. 2001; Spoon et al. 2004) has been estimated and even higher estimates from models exist (Siebenmorgen & Krügel 2007). This illustrates a limitation of our fitting procedure. The derived A_V is determined essentially from fitting the attenuation of the older stellar population, not the nuclear region. When both the 9.7 and 18.0 μm silicate absorption features are observed along with optical or near-IR stellar continuum, we could then modify our fitting procedure to first fit the A_V of a foreground screen for the H II regions + PDRs implied by the depth of the silicate absorption and then apply a second, more optically thin foreground screen to match the extinction of the older stars seen in the visible-UV part of the spectrum.

In order to test the effect on the fitting parameters, we have made such a model, which we present in Figure 20. This model,

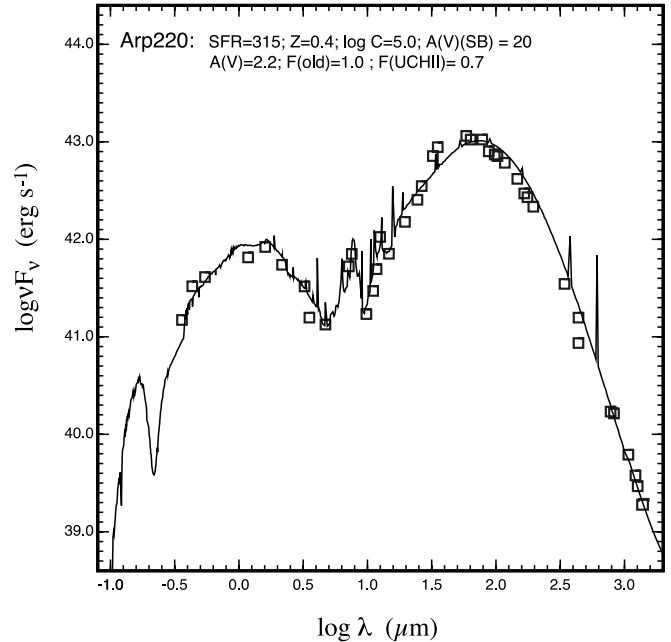


FIG. 20.—Double foreground dust screen fit to the starburst galaxy Arp 220. The screen around the starburst nucleus has $A_V = 20$ mag, and the diffuse older star component has an attenuation of $A_V = 2.2$. The fit around the silicate absorption features is improved in this more complex model. [See the electronic edition of the Supplement for a color version of this figure.]

with $A_V = 20$ mag for the starburst component and $A_V = 2.2$ for the older stars certainly fits the region of the silicate absorption features better and allows a much larger fraction of compact H II regions; $f_{\text{UCHII}} \sim 0.7$, implying that $\sim 41\%$ of all stars younger than 1.0 Myr are found in compact H II regions.

The fact that we derive a lower A_V for the starburst than other authors is not surprising, since the attenuation law that we use provides greater attenuation in the IR and less in the UV than a standard extinction law, thanks to the patchy nature of the foreground screen. What is surprising is the reduction in the strength of the emission lines in the visible and UV regions of the spectrum. This is caused by the much larger nuclear attenuation, and shows that the equivalent widths of the IR emission lines compared with the visible or near IR emission lines may be used as a sensitive diagnostic of nuclear extinction.

It should be noted that, while Arp 220 is one of the predominantly used starburst templates, there is increasing evidence that this object is not a good representative for high- z star-forming galaxies (see, e.g., Menéndez-Delmestre et al. 2007). Rather, less extreme objects such as M82 or NGC 6240 are better local analogs of the high- z actively star-forming objects such as submillimeter galaxies.

8.3. Fitting Spitzer IRS Spectra

As a final example of the fitting process, we compare our fit with the detailed *Spitzer Space Observatory* IRS low-resolution spectra of NGC 7714 from Brandl et al. (2006). The fit is shown in Figure 21. Note that this object has a much lower SFR ($8.0 M_{\odot} \text{ yr}^{-1}$) than the previous two examples. The SFR is very well constrained by the normalization process and can be determined to an accuracy of better than 5%, assuming that the IRS aperture integrates the full extent of the star-forming region.

For this object, the older stellar component is not well constrained, as the IRS spectra do not quite extend to short enough wavelengths to measure it. In addition, because the attenuation is not enough to produce appreciable 9.7 μm silicate absorption

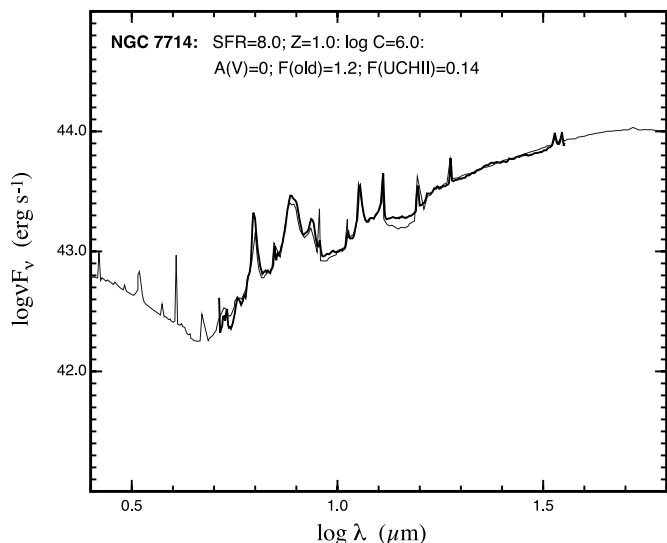


FIG. 21.—Fit to the *Spitzer Space Observatory* IRS low-resolution spectra of NGC 7714 from Brandl et al. (2006). [See the electronic edition of the Supplement for a color version of this figure.]

($A_V < 5$ mag.), we cannot measure A_V from these spectra, so it has been set equal to zero. Note that the line-emission spectrum is quite well fitted by the model, except for the strength of both the [S IV] and the [Ar III] lines in the vicinity of the $9.7 \mu\text{m}$ silicate absorption band. Again, this may indicate a rather higher obscuration of the young H II regions than in the model.

In this spectrum the abundance is fairly well constrained by the strength of the PAH features and the equivalent width of the emission lines, while the $20\text{--}35 \mu\text{m}$ slope constrains the values of $\log C$ and f_{UCHII} . The rather steep slope in the continuum spectrum at about $16 \mu\text{m}$ is a characteristic signature of the presence of compact H II regions.

9. DISCUSSION AND CONCLUSIONS

In this paper we have described an extensive library of pan-spectral SED models applicable to starburst galaxies and demonstrated the promise of these in deriving the physical parameters of starbursts. These models rely on a local, rather than a global solution to the radiative transfer. Such an approach works because of the fact that, in starburst galaxies, the vast majority of the far-IR emission arises from absorption of the UV radiation field in a relatively thin dust layer, the classical photodissociation region (PDR). This region has a typical optical depth corresponding to $A_V \sim 3$ and a thickness $\Delta R \sim 300/n_{\text{H}}$ pc. In the molecular regions surrounding normal galactic H II regions, hydrogen densities are typically $100\text{--}1000 \text{ cm}^{-3}$, implying that much of the far-IR they produce comes from a layer of parsec or subparsec dimensions. In starburst galaxies, interstellar pressures may range up to a factor of 100 higher than this, producing correspondingly thinner PDR zones. In addition, the Strömgren volume, the volume of the ionized gas in the H II region surrounding the exciting star or cluster, scales as n_{H}^{-2} , making H II regions much more compact as the pressure in the ISM is increased.

By simplifying the radiative transfer problem to a local one connected with individual clusters and their H II regions and PDRs, we can compute the SED as the sum of a set of effectively independent components. Our library of models provides the following ingredients to the pan-spectral SED of starbursts:

1. An ensemble of H II regions surrounding young clusters with ages < 10 Myr.

2. A set of PDRs surrounding these H II regions.

3. A population of young (< 1.0 Myr) ultracompact H II regions and their PDRs surrounding individual massive stars.

4. An older stellar population with ages $10 \leq t \leq 100$ Myr.

5. A foreground turbulent attenuating dust screen. Separate screens may be used for the younger < 10 Myr population and the older stellar population.

6. A reemission component from the diffuse ISM.

We have shown that the position of the far-IR dust reemission peak is primarily controlled by compactness parameter C defined in § 3, although the position and shape of this feature is also influenced by the mean covering fraction of the PDRs surrounding the individual H II regions, f_{PDR} , investigated in § 4, and by the metallicity discussed in § 7. In addition we have investigated the effect of the column density in the PDRs surrounding the H II regions, provided a global spectrum of an ensemble of compact H II regions derived from our earlier work, and have investigated the effect of metallicity on the SED of the older stars with ages $10 \leq t \leq 100$ Myr.

Finally, we have provided the attenuation properties of a turbulent absorbing dusty screen and have computed simple one-dimensional models of the thermal emission from the diffuse dust illuminated by the SED of the older (> 10 Myr) population. These models are characterized by the local diffuse radiation field intensity, expressed in units of the Habing field intensity, G_0 , where $G_0 = 1.0$ corresponds to the intensity of the diffuse radiation field in the vicinity of the Sun.

We have demonstrated how the far-IR to submillimeter SED is controlled by the compactness parameter $\log C$ and by the metallicity. This is of particular application to the high-redshift submillimeter galaxies. As shown by Blain et al. (2004), a modified blackbody fit can be made to the long-wavelength side of the far-IR peak in starburst galaxies to derive a “dust temperature.” Although the concept of such a dust temperature is physically meaningless in the light of our models, which contain a wide distribution in dust temperatures, it is a useful way to characterize the slope and the position of the submillimeter SED and may well be related to the minimum dust temperature in the starburst.

Blain et al. (2004) showed that, in ULIRGs, the dust temperature derived in this way is observed to correlate with the absolute luminosity (or, equivalently, to the SFR). In our interpretation we would conclude that for ULIRGs, the compactness parameter increases with increasing luminosity. This would be consistent with more luminous galaxies having greater surface densities of star formation and greater gas pressures and densities. This in turn is in accord with the empirical Kennicutt (1998) law of star formation; $\Sigma_{\text{SFR}} \propto \Sigma_{\text{gas}}^{1.4 \pm 0.1}$.

However, the Blain et al. (2004) work also showed that the high-redshift submillimeter-selected galaxies (SMGs) provide a similar correlation, but shifted to higher luminosity. At a given luminosity, the dust temperature in SMGs is about 20 K cooler than in ULIRGs in the local universe, and at a given dust temperature, the SMGs are typically 30 times as luminous as their ULIRG counterparts. Given that we have no reason to suspect lower dust temperatures in submillimeter galaxies, we must conclude that the starbursts in these galaxies have compactness similar to local starbursts, but are typically 30 times more luminous and spatially extended than local ULIRGs.

Tagaki et al. (2003a, 2003b) had previously found that most ULIRGs have a constant surface brightness of order $10^{12} L_{\odot} \text{ kpc}^{-2}$. These parameters probably characterize “maximal” star formation, above which gas is blown out into the halo of the galaxy and star formation quenched. In order to scale the star formation up to the

MODELING THE PAN-SPECTRAL ENERGY DISTRIBUTION OF STARBURST GALAXIES. IV.
THE CONTROLLING PARAMETERS OF THE STARBURST SED

Brent Groves,¹ Michael A. Dopita,² Ralph S. Sutherland,² Lisa J. Kewley,³ Jörg Fischer,⁴
Claus Leitherer,⁵ Bernhard Brandl,¹ and Wil van Breugel⁶

Received 2007 August 31; accepted 2007 December 8

ABSTRACT

We combine the stellar spectral synthesis code Starburst99, the nebular modeling code MAPPINGS III and a one-dimensional dynamical evolution model of H